

Structural Evolution of Core–Shell Gold Nanoclusters: Au_n^- ($n = 42–50$)

Seema Pande,[†] Wei Huang,^{‡,||} Nan Shao,[§] Lei-Ming Wang,^{‡,⊥} Navneet Khetrapal,[†] Wai-Ning Mei,[§] Tian Jian,[‡] Lai-Sheng Wang,^{*,‡} and Xiao Cheng Zeng^{*,†}

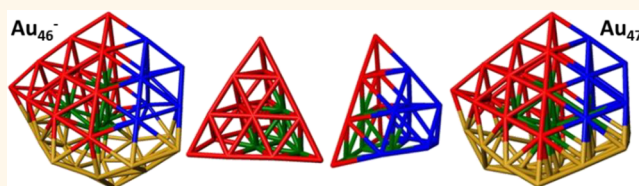
[†]Department of Chemistry, University of Nebraska-Lincoln, Lincoln, Nebraska 68588, United States

[‡]Department of Chemistry, Brown University, Providence, Rhode Island 02912, United States

[§]Department of Physics, University of Nebraska-Omaha, Omaha, Nebraska 68182, United States

Supporting Information

ABSTRACT: Gold nanoclusters have attracted great attention in the past decade due to their remarkable size-dependent electronic, optical, and catalytic properties. However, the structures of large gold clusters are still not well-known because of the challenges in global structural searches. Here we report a joint photoelectron spectroscopy (PES) and theoretical study of the structural evolution of negatively charged core–shell gold nanoclusters (Au_n^-) for $n = 42–50$. Photoelectron spectra of size-selected Au_n^- clusters are well resolved with distinct spectral features, suggesting a dominating structural type. The combined PES data and density functional calculations allow us to systematically identify the global minimum or candidates of the global minima of these relatively large gold nanoclusters, which are found to possess low-symmetry structures with gradually increasing core sizes. Remarkably, the four-atom tetrahedral core, observed first in Au_{33}^- , continues to be highly robust and is even present in clusters as large as Au_{42}^- . Starting from Au_{43}^- , a five-atom trigonal bipyramidal core appears and persists until Au_{47}^- . Au_{48}^- possesses a six-atom core, while Au_{49}^- and Au_{50}^- feature seven- and eight-atom cores, respectively. Notably, both Au_{46}^- and Au_{47}^- contain a pyramidal Au_{20} motif, which is stacked with another truncated pyramid by sharing a common 10-atom triangular face. The present study sheds light on our understanding of the structural evolution of the medium-sized gold nanoclusters, the shells and core as well as how the core–shell structures may start to embrace the golden pyramid (bulk-like) fragment.



KEYWORDS: gold nanoclusters, structural evolution, photoelectron spectroscopy, core–shell structures, gold anion clusters

Gold nanoparticles can exhibit unique physical and chemical properties that do not exist in bulk gold.^{1–4} Many of these unique properties can be attributed to both strong relativistic effects and finite-size quantum effects.^{4–7} Gold nanoparticles have received special attention in chemistry due to their exceptional catalytic properties and potential applications in various important chemical transformations.^{8–15} In particular, supported gold nanoclusters have been discovered to catalyze CO oxidation below room temperature.^{12–15} The catalytic properties are highly dependent on the size, structure, and charge state of the gold clusters.^{8,10,15} A deeper understanding of the structure-catalytic property relationship requires the structural information on size-selected clusters and their evolution as a function of size.

A variety of experimental techniques, in conjunction with global minimum searches and theoretical calculations, have been used to determine the structures of small to medium-sized gold nanoclusters, including ion mobility spectroscopy (IMS),^{16,17} trapped ion electron diffraction (TIED),^{18–21} infrared multiple-photon dissociation (IR-MPD) spectroscopy,²² and size-selected photoelectron spectroscopy

(PES).^{1,23–30} To date, the structures of small gold clusters have been well established.^{1,4} Several studies have shown that gold anion clusters exhibit two-dimensional (2D) structures up to the size of Au_{12}^- ,^{16,21,23,24} followed by shell-like and hollow-cage structures up to Au_{18}^- and then pyramidal structures from Au_{18}^- to Au_{20}^- .^{25,26} The Au_{20}^- pyramidal cluster has received extensive interest because of its highly symmetric tetrahedral structure and large HOMO–LUMO gap.^{22,27} Each triangle face of the pyramidal Au_{20}^- consists of 10 atoms, arranged like an Au(111) face, and the pyramid can be viewed as a fragment of the face-centered cubic (fcc) structure of bulk gold.

In a previous study, the Au_{25}^- cluster was found to be the smallest core–shell structure, with a single-atom core.²⁸ Furthermore, the structural evolution of gold clusters from Au_{27}^- to Au_{38}^- has been investigated by joint experimental and theoretical studies.^{18,29–32} These previous studies show that the low-symmetry core–shell structures are prevailing beyond

Received: June 30, 2016

Accepted: October 29, 2016

Published: October 30, 2016

Au_{27}^- . Notably, a highly robust tetrahedral core was found to exist over a wide size range from Au_{33}^- to Au_{38}^- .³⁰ Furthermore, the appearance of a pyramidal fragment was observed in Au_{38}^- .³⁰ To the best of our knowledge, thus far, the structures of neutral clusters of Au_{40} , Au_{44} , and Au_{50} have been investigated theoretically.^{33,34} Especially for neutral Au_{50} , the previous calculations³⁴ suggested that a hollow cage appears to be more stable than core-shell structures. The current joint PES and theoretical study indicates that core-shell structures are still highly favorable in the size range of Au_{42}^- – Au_{50}^- . Remarkably, we find that the highly robust tetrahedral core is still persistent in clusters as large as Au_{42}^- . In addition, we have found that Au_{46}^- and Au_{47}^- contain a Au_{20} pyramidal fragment and that it is stacked with another truncated pyramid such that the two share a common 10-atom triangular face. Overall, we demonstrate that the high-resolution anion PES, combined with a theoretical global search, is a viable approach to resolve atomic structures of low-symmetry metal clusters, particularly the inner core structures of the core-shell clusters, which are challenging to resolve by imaging techniques due to the coverage by the outer shells.

RESULTS AND DISCUSSION

Photoelectron spectra of Au_n^- in the size range of $n = 42$ – 50 display remarkably well-resolved peaks, which are essential for detailed comparisons with the simulated spectra, as shown in Figures 1–9 (red colored), respectively. The observed spectral

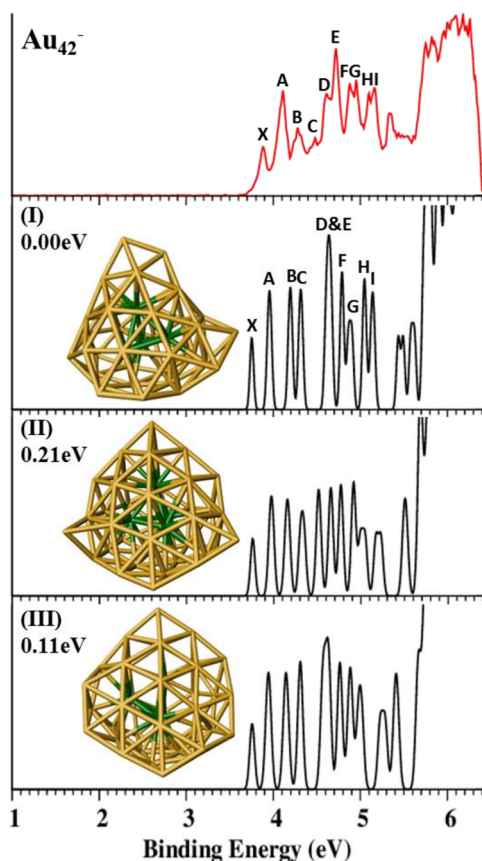


Figure 1. Photoelectron spectrum of Au_{42}^- at 193 nm (top panel, red) in comparison with the simulated spectrum (black) of isomers I–III. The core atoms of Au_{42}^- are highlighted in green in the insets.

peaks in the low binding energy range are mainly due to the 6s band and are well resolved. This spectral region is primarily used for the comparison with the simulated spectra. The lowest binding energy peak, labeled as X in each spectrum, represents the detachment transition from the anion ground state to that of the neutral. The higher binding energy peaks, labeled as A, B, C, D, *etc.*, represent detachment transitions from the ground state of the anion to the electronic excited states of the neutral. In these cases, the X–A separations represent the energy gap between the two highest occupied molecular orbitals of the anion clusters (H1–H2). Also, in some figures, weak features are labeled with *, representing the presence of minor isomer/isomers in the cluster beam.

Table 1 presents the experimental first vertical detachment energy (VDE) and the X–A gap, in comparison with the

Table 1. Experimental and Theoretical First VDEs, Experimental Gap between the First (X) and Second (A) PES Bands

cluster	first VDE (exp) ^a (eV)	X–A gap (exp) (eV)	first VDE (theo) ^b (eV)
Au_{42}^-	3.88(6)	0.23	3.75 (0.13)
Au_{43}^-	3.98(6)	0.20	3.85 (0.13)
Au_{44}^-	3.90(7)	0.26	3.67 (0.23)
Au_{45}^-	4.14(5)	0.06	3.97 (0.17)
Au_{46}^-	3.94(6)	0.23	3.70 (0.24)
Au_{47}^-	3.94(6)	0.20	3.89 (0.05)
Au_{48}^-	3.99(7)	0.20	3.90 (0.09)
Au_{49}^-	4.21(7)	0.12	4.02 (0.19)
Au_{50}^-	3.92(7)	0.36	3.61 (0.31)

^aThe number in the parentheses represents the uncertainty in the last digit. ^bThe number in the parentheses represents the red shift relative to the experimental value.

computed first VDE of the assigned isomer. As found previously, although SO-PBE0/CRENBL-ECP underestimates the VDEs of 6s band, the inclusion of SO effects is extremely important for achieving quantitative agreement between experiment and theory.^{21,29,30,35–37}

The determination of the true global minimum structures is guided by not only the DFT energetics but also a direct comparison of the simulated PES patterns (*e.g.*, number of major peaks and their relative spacing) with the experimental PES data. Among all of the leading candidates, the global minimum is identified on the basis of three criteria as mentioned in the previous study,²⁹ *i.e.*, (1) the relative energies, (2) comparison of the energy gap between the first and second peak with experiment, and (3) agreement of the distinct spectral peaks between theory and PES experiment. In Figures 1–9 we present the relative energy, calculated at the M06/cc-pVDZ-pp (ECP) level, along with simulated spectra for the leading candidates. The relative energies computed at M06/cc-pVDZ-pp (ECP) level offer additional support to these leading candidates. Because of the large size and complexity of these clusters, isomers within ~ 0.2 eV of the lowest-lying isomers and an X–A gap (at PBE level of theory) ± 0.03 eV within the experimental value are considered as the leading candidates among our top selection. To show the structural differences between the leading candidates, the plots of atom-to-center distance distributions of the leading candidate clusters are presented in Supporting Information.

Au₄₂⁻. Figure 1 displays the experimental photoelectron spectrum of Au₄₂⁻, in comparison with the simulated spectra of isomers I–III. Numerous well-resolved bands, labeled as X and A–I, are observed in the 193 nm spectrum. The well-separated PES features suggest that there is a dominating isomer in the cluster beam. The X band yields the first VDE at 3.88 eV for the dominating isomer. The energy gap between the X and A bands gives rise to a H1–H2 gap of 0.23 eV for Au₄₂⁻.

The basin-hopping (BH) search yielded a large population of candidates with the four-atom tetrahedral core. We examined nine isomers within 0.2 eV of the global minimum at the PBE/DNP/ECP (fine) level. These candidates (numbered based on their PBE/DNP/ECP (fine) energy rankings (Table S1) gave calculated energy gaps close to the experimental X–A gap 0.23 eV. Because numerous isomers were found to be close in energy for Au₄₂⁻, the relative energy values alone or the X–A gap are insufficient to determine the true global minimum. Therefore, the simulated spectra for all of the top candidates are compared with the experiment (Figure S1b).

All the top candidates, except for two, have a four-atom tetrahedral core (Table S1). Simulated spectra of these candidates are presented in Figure S1b. Isomers I–III with a tetrahedral core and almost identical first VDEs (Table S1) emerged as the best candidates, and they give similar simulated spectra which appear to agree with the experiment (Figure 1). To quantitatively compare simulated spectrum with the experimental spectrum, we align the first peak with the experimental one (X peak) and calculate the root-mean-square deviation (RMSD) for the labeled peaks A–I (top panel in Figure 1). The smallest RMSD value (0.039 eV) for isomer II implies the closest match to experimental spectrum (Table S1). The key features of the simulated spectrum of isomer I are also in quantitative agreement with experimental spectrum, except for the intense peak at ~4.6 eV which consists of closely spaced peaks. Moreover, the energy of isomer I calculated at the SO-PBE0/CRENBL/ECP level and the M06/cc-pVDZ-pp(ECP) level is the lowest among all of the isomers considered. Although isomer II also has many of the characteristic features in the simulated spectrum, it is 0.15 and 0.21 eV higher in energy in the two levels of theory than in isomer I. Considering the size and complexity of these clusters, the very good agreement between the experimental spectrum and the lower relative energy of isomer I and isomer II provides credence for our conclusion that both are the major isomer in the cluster beam. However, isomer III may be the carrier of weak features, which are buried under the main spectral features. Even though we cannot completely rule out isomer III, it is unlikely that it is a major contributor to the observed spectrum.

Au₄₃⁻. The PES spectrum of Au₄₃⁻ (Figure 2) is particularly well resolved because only doublet final states are allowed in one-electron detachment. The first VDE defined by the X band was measured to be 3.98 eV, and the energy gap between the X and A bands was measured to be 0.20 eV. The simulated spectra of isomers I–III to be presented below are shown in Figure 2 for comparison.

The BH search resulted in an equivalent population of both the four- and five-atom core candidates. We examined the ten low-lying isomers that are within 0.2 eV of the global minimum at the PBE/DNP/ECP (fine) level. Six of these candidates have a four-atom tetrahedral core and four have a five-atom trigonal bipyramidal core. The relative energies, the X–A gap, and the first VDE of these isomers are presented in Table S2.

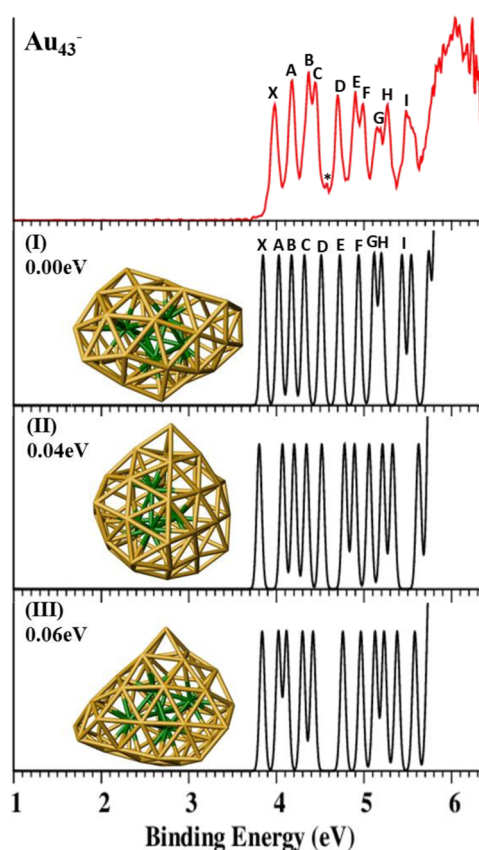


Figure 2. Experimental photoelectron spectrum of Au₄₃⁻ at 193 nm (top panel, red) in comparison with the simulated spectra (black) of isomers I–III. The core atoms of the Au₄₃⁻ isomers are highlighted in green in the insets.

Among these top candidates, isomer I is lowest in energy at the PBE/DNP/ECP (fine) level as well as the SO-PBE0/CRENBL/ECP level. The relative energy differences among isomers I–III are very small, although the simulated spectral features from isomer I seem to agree the best with the experimental spectrum (Figure 2). All of the observed spectral features X and A to I, including the broad band at ~5.5 eV, and their relative spacing are well reproduced in the simulated spectrum of isomer I. In particular, the calculated X–A gap of 0.18 eV is very close to experimental gap of 0.20 eV. The simulated spectra of isomers II and III also display numerous peaks, but the relative spacing among the peaks does not agree with the experiment compared to that of isomer I. Quantitatively the calculated RMSD value (for the labeled peaks A–I) for isomer I is the lowest among three candidates, and it affirms that the simulated spectrum of isomer I agrees well with the experimental spectrum (Table S2). The relative energies for these three isomers calculated at the M06/cc-pVDZ-pp(ECP) level are within 0.06 eV (Figure 2), and they should all be considered energetically degenerate. On the basis of the good agreement between the simulated and experimental spectrum, we conclude that isomer I with the trigonal bipyramidal core should be the dominant isomer observed experimentally.

The Au₄₃⁻ cluster is the first size, where the five-atom trigonal bipyramidal core appears. It can be viewed as the addition of an atom to the core of the Au₄₂⁻ cluster with a 38 atom shell. It also has a low symmetry (C₁) with a somewhat tubular shape comprising of all triangle facets.

Au_{44}^- . The experimental spectrum of Au_{44}^- presented in Figure 3 appears to be more complicated both because this

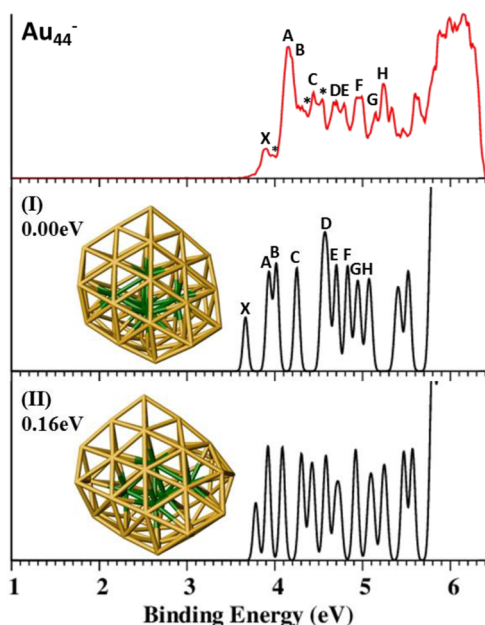


Figure 3. Photoelectron spectrum of Au_{44}^- at 193 nm (top panel, red) in comparison with the simulated spectrum (black) of isomers I and II. The core atoms of the Au_{44}^- structure are highlighted in green in the insets.

cluster is open shell and there seems to be clear evidence of contributions from other isomers (weak features labeled with *). The X band gives rise to the first VDE at 3.90 eV, and the energy gap between X and A is 0.26 eV. The strong band A seems to have a shoulder on the higher binding energy side (B).

Our global minimum search resulted in a large population of clusters with trigonal bipyramidal core. We examined 11 candidates numbered by the PBE/DNP/ECP (fine) energy rankings (see Table S3). Most of the top candidates gave rise to HOMO–LUMO gaps between 0.23 and 0.29 eV close to the experimental observation of 0.26 eV, except for isomer II.

Isomer I emerged as the best candidate with the lowest energy at the SO-PBE0/CRENBL/ECP level. In particular, for isomer I the calculated X–A gap of 0.27 eV is very close to the experimental gap of 0.26 eV. Also, the closely spaced A and B bands in the simulated spectrum of isomer I are in good agreement with the experiment (Figure 3). Isomer II is the next top candidate based on the relative energy calculated at the SO-PBE0/CRENBL/ECP level (0.16 eV higher than isomer I, Figure 3). The first VDE of isomer II is slightly higher than that of isomer I (Table S3) and agrees with the weak feature * between bands X and A. Isomer II should also contribute to the congested features at higher binding energies. It is clear that the simulated spectrum of isomer I alone would not explain all of the observed features. Isomer II should be a viable low-lying isomer, which was present in the cluster beam and contributed to the observed spectrum.

Isomers I and II both have core–shell structures with a five-atom trigonal bipyramid core and a 39-atom shell. Visually, the two structures appear to resemble one another. However, the plots of atom-to-center distance distributions reveal the structural differences better between the two isomers (Figure

S3a). The shell of isomer I contains one rhombus defect (Figure S3c), which is not present in isomer II.

Au_{45}^- . The experimental spectrum of Au_{45}^- at 193 nm (Figure 4) is well resolved as a result of its closed-shell nature.

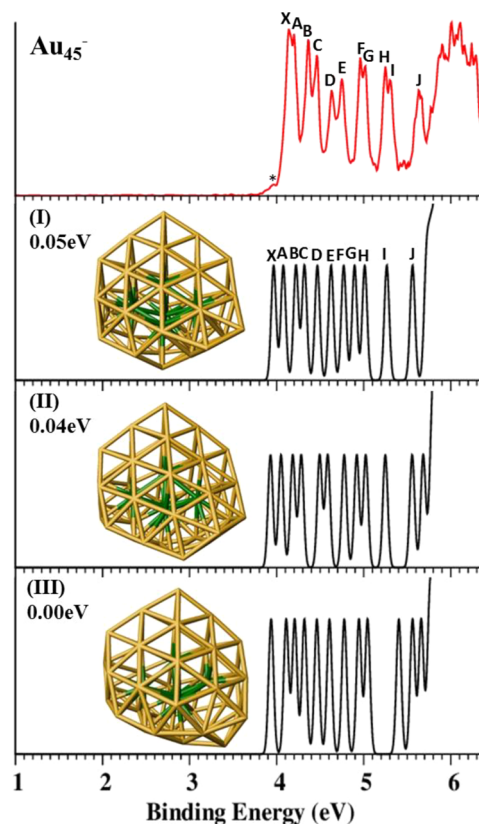


Figure 4. Photoelectron spectrum of Au_{45}^- at 193 nm (top panel, red) in comparison with the simulated spectrum (black) of isomers I–III. The core atoms of the Au_{45}^- structures are highlighted in green in the insets.

The spectrum seems to consist of closely spaced pairs of peaks, *i.e.*, X/A, B/C, D/E, F/G, and H/I. The X peak yields the first VDE at 4.14 eV. The X–A energy gap of 0.06 eV is very small. The spectrum of Au_{45}^- is quite characteristic and less congested (Figure 4), suggesting the presence of a dominant isomer. The low binding energy tail, labeled * at ~3.97 eV, suggests the presence of a possible minor isomer in the cluster beam.

We examined 13 candidates within a relative energy of 0.2 eV at PBE/DNP/ECP (fine) level (Table S4). Isomers I–III emerged as the lowest-energy structures at the SO-PBE0/CRENBL/ECP level. Their relative energies calculated at the M06/cc-pVDZ-pp(ECP) level are also very small (Figure 4).

Isomer III, which is lowest in energy at the M06 level, has features that do not agree well with experiment, specifically the X–A energy gap is relatively large (0.17 eV), and it can be readily ruled out. The simulated spectrum of isomer I produces well-defined peaks, which resemble better to the experimental spectrum. The simulated PES spectrum of isomer II also displays resemblance to the experiment, and it is lower in energy than isomer I by 0.01 eV, and they should be considered degenerate. Nevertheless, the lower RMSD value for isomer I than isomer II also suggests that isomer I is more likely the major isomer contributing to the observed spectrum. We tentatively assign isomer I with a trigonal bipyramidal core as

the global minimum. We note that isomers I–III all have a five-atom core and visually they seem to resemble closely to each other. The plots of atom-to-center distance distributions show more clearly that they represent different structures (Figure S4a). On close examination, one can see that the shell of isomer I consists of three rhombus defects (Figure S4c).

Au₄₆⁻. The photoelectron spectrum of Au₄₆⁻ at 193 nm (Figure 5) displays some similarity to that of Au₄₅⁻ (Figure 4),

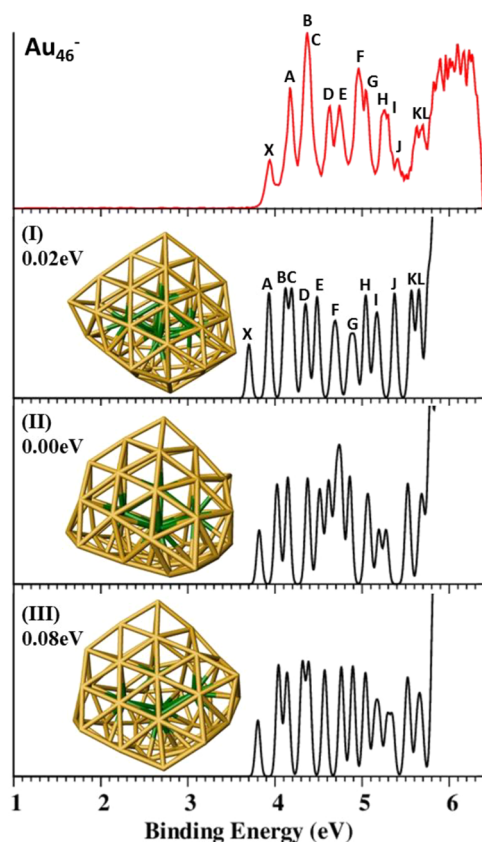


Figure 5. Photoelectron spectrum of Au₄₆⁻ at 193 nm (top panel, red) in comparison with the simulated spectrum (black) of isomers I–III. The core atoms of the Au₄₆⁻ isomers are highlighted in green in the insets.

specifically the higher energy features beyond 4.5 eV, even though the latter is closed shell. The X band defines the first VDE at 3.94 eV, followed by a more intense A band at 4.17 eV which is close to first VDE of Au₄₅⁻ (4.14 eV). The X–A energy gap of 0.23 eV represents the HOMO–LUMO gap of neutral Au₄₆. Compared with that of Au₄₄⁻, which is also open shell (Figure 3), the spectrum of Au₄₆⁻ is much better resolved with well-defined peaks, suggesting the presence of a single isomer in the cluster beam. These observations also indicate that the global minimum of Au₄₆⁻ should be significantly more stable than the nearest isomer.

We examined eight low-lying isomers ranked by energies from the PBE/DNP/ECP (fine) level (Table S5). These candidates gave calculated energy gaps between 0.20 and 0.27 eV, all close to the experimental X–A gap 0.23 eV.

Isomers I–III are lowest in energy, and they are nearly degenerate at the PBE/DND/ECP level of theory. The simulated spectrum of isomer I appears to agree best with the experimental spectrum (Figure 5). The X–A gap of isomer I (0.23 eV) is the same as observed experimentally. All of the

peaks and relative spacing resemble almost quantitatively the experimental features, lending considerable credence to the conclusion that isomer I should be the global minimum for Au₄₆⁻. Even though the three isomers are nearly degenerate from PBE/DND/ECP, isomers II and III can be ruled out on the basis of the simulated spectra. We also calculated the relative energies of the three isomers at M06/cc-pVDZ-pp(ECP) level (Figure 5). Isomer I is only 0.016 eV higher in energy than isomer II. Clearly, the relative energies alone are not sufficient to determine the true global minimum for such large and complicated systems. The global minimum isomer I of Au₄₆⁻ with a five-atom core has a quite unique structure: It consists of a distinguishable pyramid of 20 atoms, like Au₂₀,^{22,27} which is a fragment of the fcc structure of bulk gold, and it is also the stacked with a truncated pyramid (see Figure 10a below for more structural details).

Au₄₇⁻. The photoelectron spectrum of Au₄₇⁻ (Figure 6) consists of rather congested PES features with large intensity

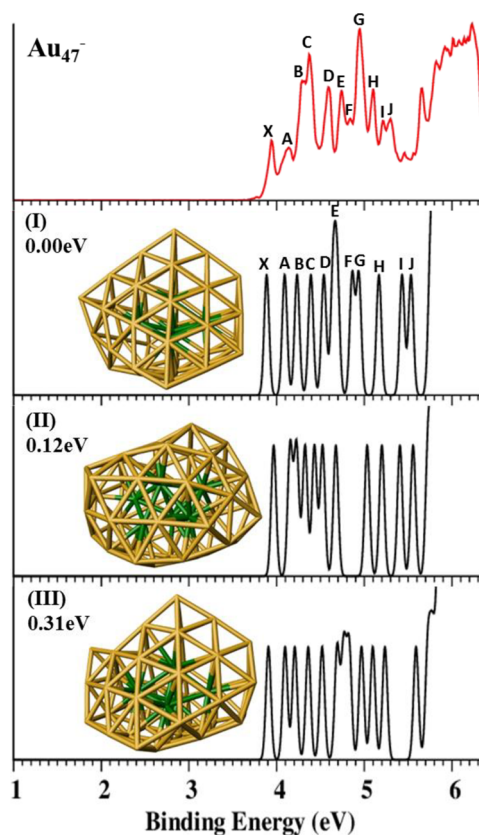


Figure 6. Photoelectron spectrum of Au₄₇⁻ at 193 nm (top panel, red) in comparison with the simulated spectrum (black) of isomers I–III. The core atoms of the Au₄₇⁻ isomers are highlighted in green in the insets.

variations, which could indicate that significant low-lying isomers might be present experimentally. The X band gives rise to the first VDE at 3.94 eV, followed by band A with similar intensity at 4.14 eV, resulting in an X–A energy gap of 0.20 eV.

Our BH search yielded isomers with both five- and six-atom core structures. We examined 10 low-lying isomers (Table S6), but only three candidates (isomers I–III) met our selection criteria, and their simulated spectra are compared with the experiment in Figure 6.

Isomer I with a five-atom core was found to be the global minimum, being lowest in energy at all levels of theory. The simulated spectrum of isomer I agrees well with the experiment and all of the characteristic features, and the spacing is well represented. The calculated X–A gap (0.21 eV) is also very close to the experimental gap (0.20 eV). It should be pointed out that the simulated spectra of isomers II and III also have some features similar to the experimental spectrum, and they could conceivably contribute to the observed spectrum, even though the energies calculated at M06/cc-pVDZ-pp level clearly show that both are higher in energy than isomer I. We tentatively assign isomer I as the global minimum of Au_{47}^- , which has a trigonal bipyramidal core. This isomer also exhibits not only the distinguished 20-atom pyramidal fragment but also the stacked truncated pyramid, similar to that of the Au_{46}^- cluster (see Figure 10 below).

Au_{48}^- . The photoelectron spectrum of Au_{48}^- (Figure 7) is well resolved, but congested spectral features are observed in

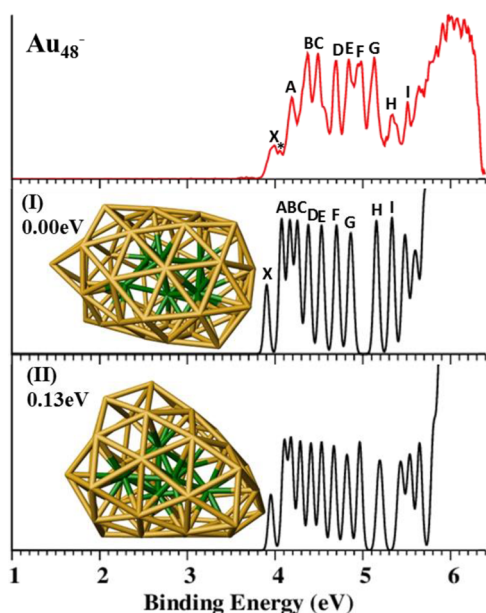


Figure 7. Photoelectron spectrum of Au_{48}^- at 193 nm (top panel, red) in comparison with the simulated spectrum (black) of isomers I and II. The core atoms of the Au_{48}^- structure are highlighted in green in the insets.

the high binding energy range (B–I). The weak feature between the X and A bands (labeled *) suggests the possibility of the existence of a low-lying isomer in the cluster beam, making minor contributions to the experimental spectrum. The X peak gives rise to the first VDE at 3.99 eV, followed by a more intense band A at 4.19 eV. The X–A energy gap of 0.20 eV represents the HOMO–LUMO gap of neutral Au_{48} .

The BH search resulted in a large population of structures with six-atom cores. We examined nine candidates ranked at the PBE/DNP/ECP (fine) level of theory (Table S7), eight candidates with six-atom cores, and one with a seven-atom core. Isomer I is lowest in energy at the SO-PBE0/CRENBL/ECP level. The simulated spectra of the top two isomers are compared with the experimental spectrum in Figure 7; both give similar and congested spectral features. The simulated spectrum of isomer I seems to match the experimental spectrum well, and quantitatively, the calculated RMSD value for the labeled peaks A–I is lower than that of isomer II (Table

S7), suggesting isomer I is more likely the major isomer in the cluster beam. In particular, the X–A gap of isomer I is also very close to experimental (Table S7). The first VDE of isomer II is slightly higher than isomer I. The simulated spectrum of isomer II also seems to reproduce certain features observed in the experiment and is likely making minor contributions to the observed spectrum, such as the weak feature labeled as *. Isomer II is 0.13 eV higher in energy than isomer I at the M06 level of theory and thus should be considered as the candidate for the minor isomer. Both isomers I and II with low symmetry (C_1) consist of a six-atom core. Au_{48}^- is the first cluster to feature the six-atom core and signals another structural transition of core expansion, similar to that in Au_{43}^- .

Au_{49}^- . The photoelectron spectrum of Au_{49}^- at 193 nm (Figure 8) consists of congested, but well-resolved features (X

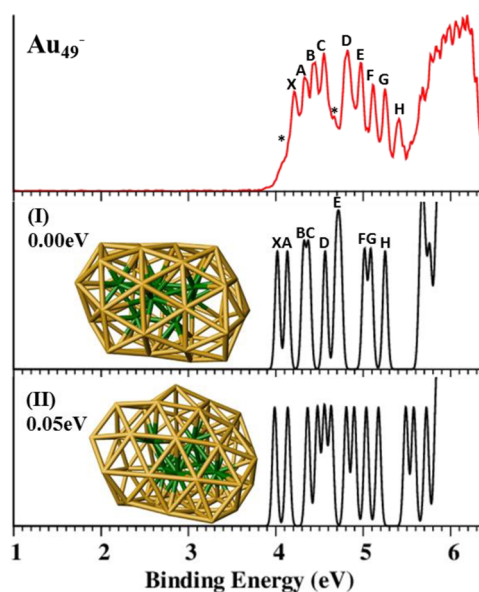


Figure 8. Photoelectron spectrum of Au_{49}^- at 193 nm (top panel, red) in comparison with the simulated spectrum (black) of isomers I and II. The core atoms of the Au_{49}^- isomers are highlighted in green in the inset.

and A to H). The X band defines the first VDE at 4.21 eV with an X–A gap of 0.12 eV. We observe two weak intensity features (labeled *), the shoulder on the low-binding energy side of the X band at ~ 4.1 and at 4.7 eV. The weak intensities suggest that they are likely from a minor isomer.

From the BH global minimum search we found a large population of six-atom core structures and small population of five- and seven-atom core structures. We examined nine candidates ranked at the PBE/DNP/ECP (fine) level of theory (Table S8). The simulated spectra of isomers I and II are compared with the experiment in Figure 8. The energies calculated at M06/cc-pVDZ-pp(ECP) level clearly show that both are low-lying isomers and should be considered degenerate (Table S8). The simulated spectra of isomer I resemble the key features of the experiment, suggesting that isomer I is likely the major isomer in the cluster beam. In particular, the X–A gap of isomer I (0.12 eV) is the same as observed experimentally. Since isomer II gives a lower first VDE and larger X–A gap (Table S8), it is likely the carrier of the weak low binding energy features labeled *. Both simulated spectra have features resembling the experiment, suggesting

that these two isomers must be present in the cluster beam and contribute to the observed spectrum. Isomers I and II have seven- and six-atom cores, respectively, suggesting that the seven-atom core becomes competitive at this size.

Au₅₀⁻. The photoelectron spectrum of Au₅₀⁻ at 193 nm is presented in Figure 9. The well-resolved X band defines the

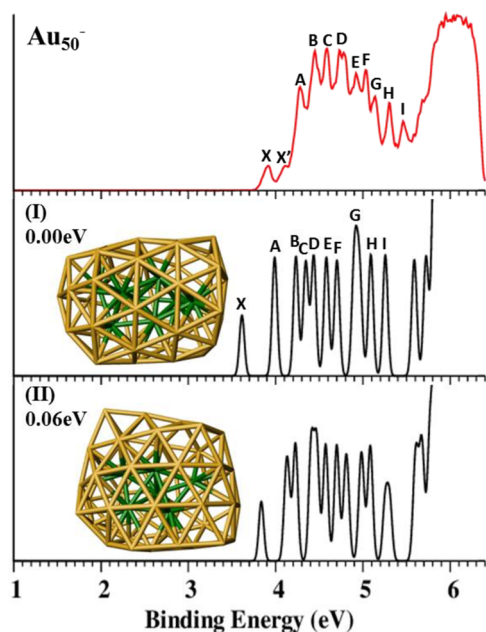


Figure 9. Photoelectron spectrum of Au₅₀⁻ at 193 nm (top panel, red) in comparison with the simulated spectrum (black) of isomers I and II. The core atoms of the Au₅₀⁻ isomers are highlighted in green in the inset.

first VDE at 3.92 eV, with a fairly large X–A gap of 0.36 eV, which represents the HOMO–LUMO gap of neutral Au₅₀. There is also a well-resolved weak peak (X') between the X and A bands at 4.01 eV, which should be due to another isomer. The similar intensities of X and X' suggest that the isomer is substantially populated. Indeed, the congested and complicated PES pattern is consistent with the presence of multiple isomers.

From the the BH global minimum search we found large populations of isomers with small energy gaps. The large X–A gap observed in the photoelectron spectrum is somewhat special in this size range. We found only six isomers fit our selection criteria (Table S9). Interestingly, these candidate structures exhibit different cores: one has a six-atom core, three have a seven-atom core, and two have an eight-atom core. Isomer I is the lowest-energy structure at the SO-PBE0/CRENNBL/ECP level; its simulated spectrum reproduces quite well the key experimental features of X and A–I. In particular, the X–A gap of isomer I (0.36 eV) is the same as observed experimentally, suggesting that isomer I should be the major isomer in the cluster beam. The first VDE of isomer II is slightly higher than that of isomer I, and it should be responsible for the X' band. In fact, the first peaks of the simulated spectrum of isomer II agree well with bands X', suggesting that isomer II must also be present in the cluster beam. Furthermore, isomers I and II are within 0.06 eV at the M06/cc-pVDZ-pp(ECP) level and should be considered energetically degenerate.

Both isomers I and II have low symmetries (C₁). Isomer I has a somewhat elongated shape with an eight-atom core, and

isomer II has a more globular shape with a six-atom core. On close examination, one can see that the shell of isomer I consists of two pentagon defects (Figure S9c). A hollow cage structure has been suggested for neutral Au₅₀ with a large HOMO–LUMO gap of 0.831 eV,³⁴ much higher than that observed in the current experiment (0.36 eV). We did not find any hollow structures in our global searches for Au₅₀⁻, and all our candidates from the BH search are composed of core–shell-type structures.

Structural Evolution from Au₄₂⁻ to Au₅₀⁻. Our combined experimental and theoretical results suggest that the gold anion clusters in the size ranging from 42 to 50 atoms are low-symmetry, core–shell structures. The identified global minima for all of the clusters are compared in Figure 10a. The structural evolution in this size range takes place both *via* core and shell expansions. The robust tetrahedral core first observed in Au₃₃⁻ still exists in Au₄₂⁻, but beyond Au₄₂⁻, the clusters grow more readily by core expansion. The five-atom core of Au₄₃⁻ is trigonal bipyramid and is persistent in the global minima of Au₄₃⁻ to Au₄₇⁻. The global minimum Au₄₈⁻ possess a six-atom core, while Au₄₉⁻ and Au₅₀⁻ feature seven- and eight-atom cores, respectively. Also, the minor isomers of the latter three feature six-atom cores, suggesting different cores become competitive in this size range. The structure evolution of the gold cores in the identified global minima in the size range studied is depicted in Figure 10b. Notably, the highly robust tetrahedral core evolves into a triangular bipyramidal core for *n* = 43–47, and then low-symmetry and elongated cores for *n* = 48–50. The latter three clusters become slightly elongated in shape as well, compatible with their core shape. This is similar to the pattern indicated by Huang *et al.* for understanding the growth of large Au_{*n*}⁻ clusters, where the surface reconstruction of Au₅₈⁻ structure resulted in voids in the interior of the clusters, which was attributed to strong relativistic effects of gold atoms.³⁸ The relativistic effects are also responsible for the deviation of the geometrical structures (predicted based on comparing with experimental PES spectra) from the global-minimum structures predicted based on the Lennard-Jones, Morse, or Gupta potentials for gold clusters. The latter global-minimum structures typically have higher number of core atoms, as these potential functions favor maximum number of atom–atom contacts.³⁹

Interestingly, the Au₄₆⁻ and Au₄₇⁻ clusters are found to contain the tetrahedral pyramidal fragment similar to Au₂₀⁻.^{26,27} The tetrahedral Au₂₀ fragment was first observed in the Au₃₈⁻ cluster.³⁰ The structure of Au₄₆⁻ in fact contains two stacked pyramidal fragments. The Au₂₀⁻ fragment sharing a 10-atom face with a truncated pyramid (see Figure 10a, the red and blue highlights). It is noteworthy that the Au₄₇⁻ cluster contains similar tetrahedral fragments (see red and blue highlights): The additional atom does not complete the second pyramid (blue). Au₄₈⁻ grows by core expansion and does not have the tetrahedral fragment anymore; the addition of an atom to the core results in rearrangement of the outer shell. These low-symmetry global structures have low coordination sites on the cluster surface. Defects and low coordinated sites are known to be associated with catalytic activities of the gold nanoparticles.^{14,40} The isolated clusters should be the starting point for supported clusters in real world catalysts. It has been reported that Au₅₈⁻ is a robust core–shell cluster, and larger clusters nucleate on the surface of Au₅₈⁻ at least up to Au₆₄⁻.³⁸ It would be interesting to elucidate how gold clusters evolve beyond Au₅₀⁻ up to the robust Au₅₈⁻.

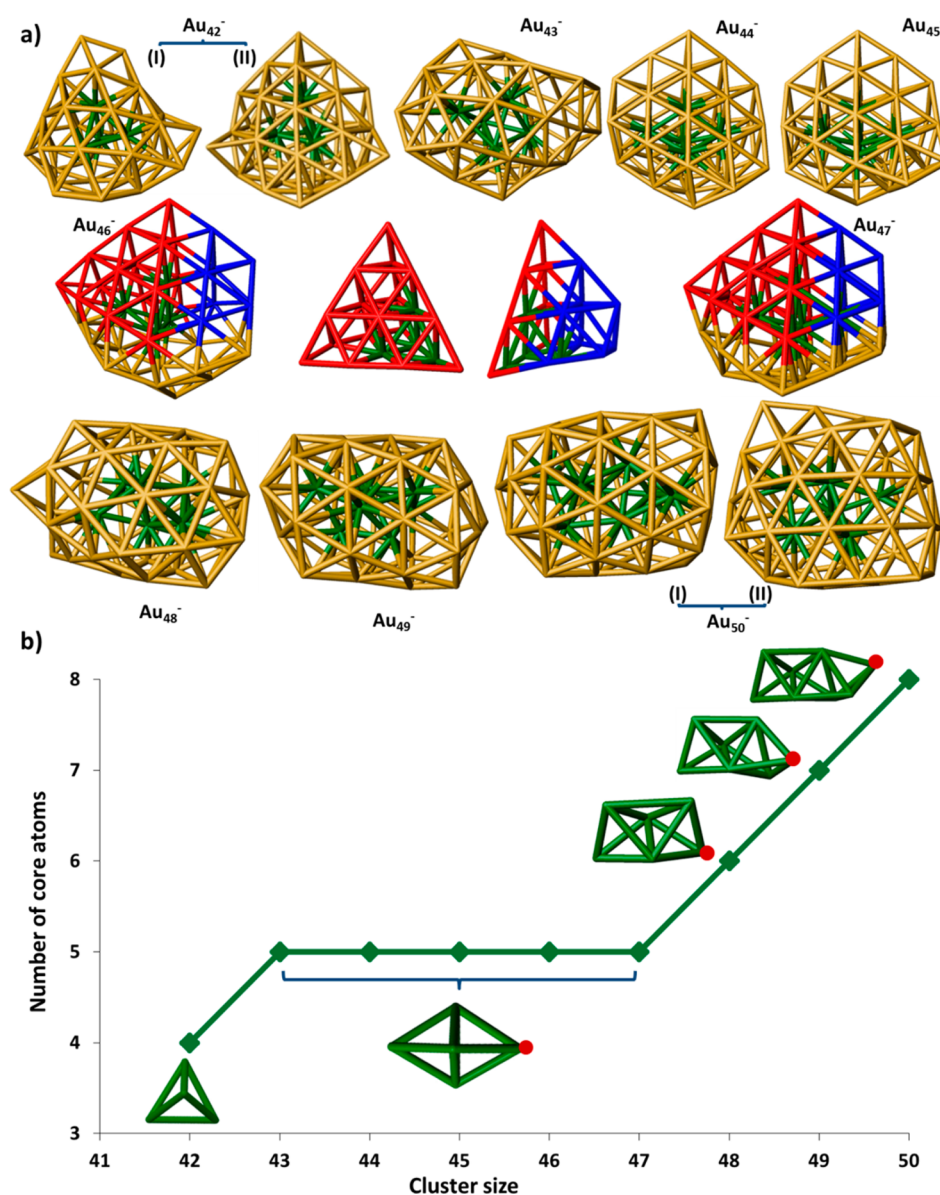


Figure 10. (a) The identified global minima of Au_n^- nanoclusters from $n = 42$ –50. Red and blue atoms highlight the pyramidal fragments in Au_{46}^- and Au_{47}^- . (b) A plot showing the gold core evolution from $n = 42$ –50. Red spheres in the core structures highlight the new gold atom added as the size of clusters increases.

CONCLUSION

We present a combined experimental and theoretical study of gold anion clusters, Au_n^- ($n = 42$ –50). The global minimum structures in this size range continue to be the low-symmetry core–shell-type. The four-atom tetrahedral core that first appeared in Au_{33}^- is found to be highly robust and is observed in the global minimum of Au_{42}^- . The global minima of Au_n^- ($n = 43$ –47) are found to contain the five-atom trigonal bipyramidal core. A core expansion is observed at Au_{48}^- which contain a six-atom core, while Au_{49}^- and Au_{50}^- feature seven-atom and eight-atom cores, respectively. The minor isomers of these three feature a six-atom core. The global minima of Au_{46}^- and Au_{47}^- are found to contain the 20-atom pyramidal fragments. This fragment is stacked with a truncated pyramidal fragment, and they share a common 10-atom triangular face. This structural information on low-symmetry core–shell gold clusters in medium-size range could be important for catalysis.

METHODS

Photoelectron Spectroscopy. The experiment was done using a magnetic-bottle PES apparatus equipped with a laser vaporization supersonic cluster source and a time-of-flight mass analyzer, details of which appear elsewhere.^{41,42} A gold disk was used as the laser vaporization target by a focused laser beam at 532 nm from a pulsed Nd:YAG laser. A high-pressure helium gas seeded with 5% Ar was used to cool the laser-induced plasma to initiate nucleation and as the carrier gas for the subsequent supersonic expansion to produce cold cluster beams. While the temperatures of the clusters were not exactly known in the cluster beam, previous experiences suggested temperatures well below 300 K.⁴³ In particular, the Ar-seeded helium carrier gas has been shown to be able to produce cold gold cluster anions by the generation of Au_n^-/Ar van der Waals complexes for planar gold cluster anions.²⁴ Ar tagging was much more difficult on the 3D clusters, even under the cold conditions by using the Ar-seeded helium carrier gas. The cold gold anion clusters were extracted perpendicularly into the time-of-flight mass spectrometer for mass analyses. The clusters of interest were selected by a mass-gate and decelerated before being photodetached in the interaction zone of the magnetic-bottle

electron analyzer. For the current experiment, the 193 nm (6.424 eV) radiation from an ArF excimer laser was used for photodetachment. Photoelectrons were collected by the magnetic bottle with nearly 100% efficiency and analyzed in a 3.5 m long time-of-flight tube. The photoelectron kinetic energies (E_k) were calibrated by the known spectra of Au⁻ and were subtracted from the photon energy to obtain the electron binding energy (BE) spectra to be presented. The resolution of the magnetic-bottle analyzer was $\Delta E_k/E_k \sim 2.5\%$, i.e., 25 meV for 1 eV electrons.

Theoretical Methods. We performed global minimum searches for the low-lying isomers of gold anion clusters (Au_n⁻) with $n = 42$ –50 atoms, using the BH global optimization method^{44–46} combined with density functional theory (DFT) calculations. The gradient-corrected Perdew–Burke–Ernzerhof (PBE) exchange–correlation functional⁴⁷ and the double-numerical polarized (DNP) basis set with effective core potential (ECP), as implemented in the DMol3 4.0 software,^{48,49} were employed for the geometry optimization. The ECP replaces the core electrons that account for the relativistic effects, whereas the (5s²5p⁶5d¹⁰6s¹) electrons were taken as valence electrons in the calculations. For the initial BH searches, we used a medium-level convergence criterion of 2×10^{-5} Ha in the DFT computations. The isomers obtained at the medium level were then reoptimized with a finer energy convergence of 1×10^{-5} Ha in DMol3.

We have collected more than 700 isomers, each for clusters from Au₄₂⁻ to Au₄₉⁻, and more than 1000 isomers for Au₅₀⁻. The candidate isomers within 0.4 eV from the lowest-energy isomer (PBE/DNP/ECP level) and the energy gap between the first and second peak (equivalent to the HOMO–LUMO gap for even sized-clusters) are selected for comparison with the experiment. These candidate isomers are optimized again using the PBE/TZP (triple- ζ polarization) level of theory with inclusion of the relativistic effects under zeroth-order regular approximation, as implemented in the ADF2013 software package.^{50–53} The single-point energies of the optimized candidate isomers are then computed at the SO-PBE0/CRENBL level of theory using the NWChem 6.3 software package.⁵⁴ Single-point energies of the neutral clusters are also computed based on the same optimized geometry. The difference in the energy of the anion and neutral cluster gives the first VDE. The first VDE is then added to the orbital energies of the deeper occupied orbitals to obtain VDEs of the higher detachment channels. The VDEs so obtained are fitted with unit-area Gaussians of 0.04 eV widths to yield the simulated spectra, which are used to compare with the experimental spectra. Lastly, we also compute relative energies among the top three to five candidate isomers using the M06 functional and cc-pVDZ-pp(ECP) basis set, as implemented in the Gaussian 09 software.⁵⁵ The M06 functional has been shown to give more accurate energy rankings among isomers of bare gold clusters, as reported previously.⁵⁶

ASSOCIATED CONTENT

Supporting Information

The Supporting Information is available free of charge on the ACS Publications website at DOI: 10.1021/acsnano.6b04330.

It includes energy tables, simulated and experimental photoelectron spectra and the Cartesian coordinates of the top-candidate isomers (PDF)

AUTHOR INFORMATION

Corresponding Authors

*E-mail: Lai-Sheng_Wang@Brown.edu.

*E-mail: xzeng1@unl.edu.

Present Addresses

^{||}Laboratory of Atmospheric Physico-Chemistry, Anhui Institute of Optics and Fine Mechanics, Chinese Academy of Sciences, Hefei, Anhui 230031, China

[†]Konica Minolta Laboratory USA, Inc., 2855 Campus Dr. Suite 100, San Mateo, CA 94403.

Notes

The authors declare no competing financial interest.

ACKNOWLEDGMENTS

The experiment done at Brown University was supported by the National Science Foundation (CHE-1632813 to L.S.W.). X.C.Z. was supported by a grant from Nebraska Center for Energy Sciences Research. The calculations were done in the Holland Computing Center at University of Nebraska-Lincoln.

REFERENCES

- (1) Wang, L.-M.; Wang, L.-S. Probing the Electronic Properties and Structural Evolution of Anionic Gold Clusters in the Gas Phase. *Nanoscale* **2012**, *4*, 4038–4053.
- (2) Daniel, M. C.; Astruc, D. Gold Nanoparticles: Assembly, Supramolecular Chemistry, Quantum-Size-Related Properties, and Applications Toward Biology, Catalysis, and Nanotechnology. *Chem. Rev.* **2004**, *104*, 293–346.
- (3) Hutchings, G. J.; Brust, M.; Schmidbaur, H. Gold—an Introductory Perspective. *Chem. Soc. Rev.* **2008**, *37*, 1759–1765.
- (4) Häkkinen, H. Atomic and Electronic Structure of Gold Clusters: Understanding Flakes, Cages and Superatoms from Simple Concepts. *Chem. Soc. Rev.* **2008**, *37*, 1847.
- (5) Gorin, D. J.; Toste, F. D. Relativistic Effects in Homogeneous Gold Catalysis. *Nature* **2007**, *446*, 395–403.
- (6) Pyykkö, P. Theoretical Chemistry of Gold. II. *Inorg. Chim. Acta* **2005**, *358*, 4113–4130.
- (7) Häkkinen, H.; Moseler, M.; Kostko, O.; Morgner, N.; Hoffmann, M. A.; Issendorff, B. V. Symmetry and Electronic Structure of Noble-Metal Nanoparticles and the Role of Relativity. *Phys. Rev. Lett.* **2004**, *93*, 93401.
- (8) Haruta, M. Size- and Support-Dependency in the Catalysis of Gold. *Catal. Today* **1997**, *36*, 153–166.
- (9) Zhang, Y.; Cui, X.; Shi, F.; Deng, Y. Nano-Gold Catalysis in Fine Chemical Synthesis. *Chem. Rev.* **2012**, *112*, 2467–2505.
- (10) Chen, M. S.; Goodman, D. W. Structure-Activity Relationships in Supported Au Catalysts. *Catal. Today* **2006**, *111*, 22–33.
- (11) Valden, M.; Lai, X.; Goodman, D. W. W. Onset of Catalytic Activity of Gold Clusters on Titania with the Appearance of Nonmetallic Properties. *Science* **1998**, *281*, 1647–1650.
- (12) Haruta, M.; Tsubota, S.; Kobayashi, T.; Kageyama, H.; Genet, M. J.; Delmon, B. Low-Temperature Oxidation of CO over Gold Supported on TiO₂, α -Fe₂O₃, and Co₃O₄. *J. Catal.* **1993**, *144*, 175–192.
- (13) Haruta, M.; Kobayashi, T.; Sano, H.; Yamada, N. Novel Gold Catalysts for the Oxidation of Carbon Monoxide at a Temperature Far below 0°C. *Chem. Lett.* **1987**, *16*, 405–408.
- (14) Lopez, N.; Janssens, T. V. W.; Clausen, B. S.; Xu, Y.; Mavrikakis, M.; Bliigaard, T.; Nørskov, J. K. On the Origin of the Catalytic Activity of Gold Nanoparticles for Low-Temperature CO Oxidation. *J. Catal.* **2004**, *223*, 232–235.
- (15) Li, L.; Gao, Y.; Li, H.; Zhao, Y.; Pei, Y.; Chen, Z.; Zeng, X. C. CO Oxidation on TiO₂ (110) Supported Subnanometer Gold Clusters: Size and Shape Effects. *J. Am. Chem. Soc.* **2013**, *135*, 19336–19346.
- (16) Furche, F.; Ahlrichs, R.; Weis, P.; Jacob, C.; Gilb, S.; Bierweiler, T.; Kappes, M. M. The Structures of Small Gold Cluster Anions as Determined by a Combination of Ion Mobility Measurements and Density Functional Calculations. *J. Chem. Phys.* **2002**, *117*, 6982–6990.
- (17) Weis, P. Structure Determination of Gaseous Metal and Semi-Metal Cluster Ions by Ion Mobility Spectrometry. *Int. J. Mass Spectrom.* **2005**, *245*, 1–13.
- (18) Lechtken, A.; Schooss, D.; Stairs, J. R.; Blom, M. N.; Furche, F.; Morgner, N.; Kostko, O.; Von Issendorff, B.; Kappes, M. M. Au₃₄: A Chiral Gold Cluster? *Angew. Chem., Int. Ed.* **2007**, *46*, 2944–2948.

- (19) Lechtken, A.; Neiss, C.; Kappes, M. M.; Schooss, D. Structure Determination of Gold Clusters by Trapped Ion Electron Diffraction: $Au_{14}^- - Au_{19}^-$. *Phys. Chem. Chem. Phys.* **2009**, *11*, 4344–4350.
- (20) Xing, X.; Yoon, B.; Landman, U.; Parks, J. H. Structural Evolution of Au Nanoclusters: From Planar to Cage to Tubular Motifs. *Phys. Rev. B: Condens. Matter Mater. Phys.* **2006**, *74*, 165423.
- (21) Johansson, M. P.; Lechtken, A.; Schooss, D.; Kappes, M. M.; Furche, F. 2D-3D Transition of Gold Cluster Anions Resolved. *Phys. Rev. A: At., Mol., Opt. Phys.* **2008**, *77*, 53202.
- (22) Gruene, P.; Rayner, D. M.; Redlich, B.; van der Meer, A. F. G.; Lyon, J. T.; Meijer, G.; Fielicke, A. Structures of Neutral Au_7 , Au_{19} , and Au_{20} Clusters in the Gas Phase. *Science* **2008**, *321*, 674–676.
- (23) Hakkinen, H.; Yoon, B.; Landman, U.; Li, X.; Zhai, H. J.; Wang, L. S. On the Electronic and Atomic Structures of Small Au_N^- ($N = 4-14$) Clusters: A Photoelectron Spectroscopy and Density-Functional Study. *J. Phys. Chem. A* **2003**, *107*, 6168–6175.
- (24) Huang, W.; Wang, L.-S. Probing the 2D to 3D Structural Transition in Gold Cluster Anions Using Argon Tagging. *Phys. Rev. Lett.* **2009**, *102*, 153401.
- (25) Bulusu, S.; Li, X.; Wang, L.-S.; Zeng, X. C. Evidence of Hollow Golden Cages. *Proc. Natl. Acad. Sci. U. S. A.* **2006**, *103*, 8326–8330.
- (26) Huang, W.; Bulusu, S.; Pal, R.; Zeng, X. C.; Wang, L. S. Structural Transition of Gold Nanoclusters: From the Golden Cage to the Golden Pyramid. *ACS Nano* **2009**, *3*, 1225–1230.
- (27) Li, J.; Li, X.; Zhai, H.-J.; Wang, L.-S. Au_{20} : A Tetrahedral Cluster. *Science* **2003**, *299*, 864–867.
- (28) (a) Bulusu, S.; Li, X.; Wang, L. S.; Zeng, X. C. Structural Transitions from Pyramidal to Fused Planar to Tubular to Core/shell Compact in Gold Clusters: Au_n^- ($n = 21-25$). *J. Phys. Chem. C* **2007**, *111*, 4190–4198. (b) Schaefer, B.; Pal, R.; Khetrpal, N. S.; Amsler, M.; Sadeghi, A.; Blum, V.; Zeng, X. C.; Goedecker, S.; Wang, L. S. Isomerism and Structural Fluxionality in the Au_{26} and Au_{26}^- Nanoclusters. *ACS Nano* **2014**, *7*, 7413–7422.
- (29) Shao, N.; Huang, W.; Gao, Y.; Wang, L. M.; Li, X.; Wang, L. S.; Zeng, X. C. Probing the Structural Evolution of Medium-Sized Gold Clusters: Au_n^- ($n = 27-35$). *J. Am. Chem. Soc.* **2010**, *132*, 6596–6605.
- (30) Shao, N.; Huang, W.; Mei, W. N.; Wang, L. S.; Wu, Q.; Zeng, X. C. Structural Evolution of Medium-Sized Gold Clusters Au_n^- ($n = 36, 37, 38$): Appearance of Bulk-like Face Centered Cubic Fragment. *J. Phys. Chem. C* **2014**, *118*, 6887–6892.
- (31) Gu, X.; Bulusu, S.; Li, X.; Zeng, X. C.; Li, J.; Gong, X. G.; Wang, L. S. Au_{34}^- : A Fluxional Core-Shell Cluster. *J. Phys. Chem. C* **2007**, *111*, 8228–8232.
- (32) Santizo, I. E.; Hidalgo, F.; Pérez, L. A.; Noguez, C.; Garzón, I. L. Intrinsic Chirality in Bare Gold Nanoclusters: The Au_{34}^- Case. *J. Phys. Chem. C* **2008**, *112*, 17533–17539.
- (33) Jiang, D. E.; Walter, M. Au_{40} : A Large Tetrahedral Magic Cluster. *Phys. Rev. B: Condens. Matter Mater. Phys.* **2011**, *84*, 84.
- (34) Wang, J.; Jellinek, J.; Zhao, J.; Chen, Z.; King, R. B.; von Rague Schleyer, P. Hollow Cages versus Space-Filling Structures for Medium-Sized Gold Clusters: The Spherical Aromaticity of the Au_{50} Cage. *J. Phys. Chem. A* **2005**, *109*, 9265–9269.
- (35) Huang, W.; Bulusu, S.; Pal, R.; Zeng, X. C.; Wang, L.-S. CO Chemisorption on the Surfaces of the Golden Cages. *J. Chem. Phys.* **2009**, *131*, 234305.
- (36) Wang, L.-M.; Pal, R.; Huang, W.; Zeng, X. C.; Wang, L.-S. Observation of Earlier Two-to-Three Dimensional Structural Transition in Gold Cluster Anions by Isoelectronic Substitution: MAu_n^- ($n = 8-11$; $M = Ag, Cu$). *J. Chem. Phys.* **2010**, *132*, 114306.
- (37) Khetrpal, N. S.; Jian, T.; Pal, R.; Lopez, G. V.; Pande, S.; Wang, L.-S.; Zeng, X. C. Probing the Structures of Gold–Aluminum Alloy Clusters $Au_x Al_y^-$: A Joint Experimental and Theoretical Study. *Nanoscale* **2016**, *8*, 9805–9814.
- (38) Huang, W.; Ji, M.; Dong, C. D.; Gu, X.; Wang, L. M.; Gong, X. G.; Wang, L. S. Relativistic Effects and the Unique Low-Symmetry Structures of Gold Nanoclusters. *ACS Nano* **2008**, *2*, 897–904.
- (39) Schwerdtfeger, P. Gold Goes Nano - From Small Clusters to Low-Dimensional Assemblies. *Angew. Chem., Int. Ed.* **2003**, *42*, 1892–1895.
- (40) Gao, Y.; Shao, N.; Pei, Y.; Chen, Z.; Zeng, X. C. Catalytic Activities of Subnanometer Gold Clusters (Au_{16} – Au_{18} , Au_{20} and Au_{27} – Au_{35}) for CO Oxidation. *ACS Nano* **2011**, *5*, 7818–7829.
- (41) Wang, L. S.; Cheng, H.-S.; Fan, J. Photoelectron Spectroscopy of Size-Selected Transition Metal Clusters: Fe_n^- , $n = 3-24$. *J. Chem. Phys.* **1995**, *102*, 9480–9493.
- (42) Wang, L.-S. Photoelectron Spectroscopy of Size-Selected Boron Clusters: From Planar Structures to Borophenes and Borospherenes. *Int. Rev. Phys. Chem.* **2016**, *35*, 69–142.
- (43) Akola, J.; Manninen, M.; Hakkinen, H.; Landman, U.; Li, X.; Wang, L.-S. Photoelectron Spectra of Aluminum Cluster Anions: Temperature Effects and *Ab Initio* Simulations. *Phys. Rev. B: Condens. Matter Mater. Phys.* **1999**, *60*, R11297–R11300.
- (44) Wales, D.; Doye, J. P. K. Global Optimization by Basin-Hopping and the Lowest Energy Structures of Lennard-Jones Clusters Containing up to 110 Atoms. *J. Phys. Chem. A* **1997**, *101*, 5111–5116.
- (45) Wales, D. J.; Scheraga, H. A. Global Optimization of Clusters, Crystals, and Biomolecules. *Science* **1999**, *285*, 1368–1372.
- (46) Yoo, S.; Zeng, X. C. Structures and Stability of Medium-Sized Silicon Clusters. III. Reexamination of Motif Transition in Growth Pattern from Si_{15} to Si_{20} . *J. Chem. Phys.* **2005**, *123*, 164303.
- (47) Perdew, J.; Burke, K.; Ernzerhof, M. Generalized Gradient Approximation Made Simple. *Phys. Rev. Lett.* **1996**, *77*, 3865–3868.
- (48) Delley, B. An All-Electron Numerical Method for Solving the Local Density Functional for Polyatomic Molecules. *J. Chem. Phys.* **1990**, *92*, 508–517.
- (49) Delley, B. From Molecules to Solids with the DMol³ Approach. *J. Chem. Phys.* **2000**, *113*, 7756–7764.
- (50) te Velde, G.; Bickelhaupt, F. M.; Baerends, E. J.; Fonseca Guerra, C.; van Gisbergen, S. J. a.; Snijders, J. G.; Ziegler, T.; Velde, G. T. E.; Guerra, C. F.; Gisbergen, S. J. a. v. a. N. Chemistry with ADF. *J. Comput. Chem.* **2001**, *22*, 931–967.
- (51) Fonseca Guerra, C.; Snijders, J. G.; Te Velde, G.; Baerends, E. J. Towards an Order-N DFT Method. *Theor. Chem. Acc.* **1998**, *99*, 391–403.
- (52) ADF; Software for Chemistry and Materials (SCM): Vrije Universiteit, Theoretical Chemistry: Amsterdam, The Netherlands, 2013; <http://www.scm.com>
- (53) Pykko, E. Relativistic Effects in Structural Chemistry. *Chem. Rev.* **1988**, *88*, 563–594.
- (54) Valiev, M.; Bylaska, E. J.; Govind, N.; Kowalski, K.; Straatsma, T. P.; Van Dam, H. J. J.; Wang, D.; Nieplocha, J.; Apra, E.; Windus, T. L.; De Jong, W. A. NWChem: A Comprehensive and Scalable Open-Source Solution for Large Scale Molecular Simulations. *Commun. Commun.* **2010**, *181*, 1477–1489.
- (55) Frisch, M. J.; Trucks, G. W.; Schlegel, H. B.; Scuseria, G. E.; Robb, M. A.; Cheeseman, J. R.; Scalmani, G.; Barone, V.; Mennucci, B.; Petersson, G. A.; Nakatsuji, H.; Caricato, M.; Li, X.; Hratchian, H. P.; Izmaylov, A. F.; Bloino, J.; Zheng, G.; Sonnenberg, J. L.; Hada, M.; Ehara, M.; Toyota, K.; Fukuda, R.; Hasegawa, J.; Ishida, M.; Nakajima, T.; Honda, Y.; Kitao, O.; Nakai, H.; Vreven, T.; Montgomery, J. A., Jr.; Peralta, J. E.; Ogliaro, F.; Bearpark, M.; Heyd, J. J.; Brothers, E.; Kudin, K. N.; Staroverov, V. N.; Kobayashi, R.; Normand, J.; Raghavachari, K.; Rendell, A.; Burant, J. C.; Iyengar, S. S.; Tomasi, J.; Cossi, M.; Rega, N.; Millam, J. M.; Klene, M.; Knox, J. E.; Cross, J. B.; Bakken, V.; Adamo, C.; Jaramillo, J.; Gomperts, R.; Stratmann, R. E.; Yazyev, O.; Austin, A. J.; Cammi, R.; Pomelli, C.; Ochterski, J. W.; Martin, R. L.; Morokuma, K.; Zakrzewski, V. G.; Voth, G. A.; Salvador, P.; Dannenberg, J. J.; Dapprich, S.; Daniels, A. D.; Farkas, Ö.; Foresman, J. B.; Ortiz, J. V.; Cioslowski, J.; Fox, D. J. *Gaussian 09*, Revision D.02; Gaussian, Inc.: Wallingford, CT, 2009.
- (56) Mantina, M.; Valero, R.; Truhlar, D. G. Validation Study of the Ability of Density Functionals to Predict the Planar-to-Three-Dimensional Structural Transition in Anionic Gold Clusters. *J. Chem. Phys.* **2009**, *131*, 064706.